Michael D. Atkins[1]
School of Mechanical, Industrial & Aeronautical Engineering,
University of the Witwatersrand,
Johannesburg 2000, South Africa
e-mail: Michael.Atkins@wits.ac.za

Frank W. Kienhöfer
School of Mechanical, Industrial & Aeronautical Engineering,
University of the Witwatersrand,
Johannesburg 2000, South Africa
e-mail: Frank.Kienhofer@wits.ac.za

Tian Jian Lu
State Key Laboratory of Mechanics and Control of Mechanical Structures,
Nanjing University of Aeronautics and Astronautics,
Nanjing, Jiangsu Province 210016, China
e-mail: tjlu@nuaa.edu.cn

Tongbeum Kim
College of Aerospace Engineering,
Nanjing University of Aeronautics and Astronautics,
Nanjing, Jiangsu Province 210016, China
e-mail: tongbeum.kim@nuaa.edu.cn

Local Heat Transfer Distributions Within a Rotating Pin-Finned Brake Disk

This study presents local temperature and heat transfer coefficient distributions obtained experimentally on the internal surfaces of a rotating pin-finned brake rotor at realistic rotation speeds for braking (i.e., $N = 100–300$ rpm). To this end, the thermochromic liquid crystal technique in a rotating reference frame was employed. The results demonstrate that the bulk airflow within the ventilated channel of a rotating disk follows a predominantly backward sweeping inline-like path between the pin fins. Internal local heat transfer is distributed nonuniformly on both inboard and outboard surfaces, with twice higher average cooling from the outboard surface than the inboard surface: this possibly exacerbates the thermal stresses, which leads to thermal distortion of the rotor (i.e., coning). [DOI: 10.1115/1.4047836]

Introduction

Automobiles typically use friction disk brakes to dissipate the kinetic energy of the vehicle, which raises the internal energy of the brake system and causes the temperature of the brake components to increase [1]. Vehicle braking results from the clamping of a rotating disk brake rotor with a caliper and brake pads, as shown in Fig. 1. Under heavy continuous braking conditions, excessive temperatures can develop (~500 °C) within the brake components that can have detrimental effects on braking performance and reliability of brake system components [2,3]. For example, such excessive brake temperatures can lead to brake fade, thus reducing the available braking torque [2,4]. Excessive and nonuniform temperatures within the brake rotor may also cause thermal distortion (e.g., coning), or cracking of the rotor, and accelerate the wear of brake pads [2–6]. To reduce the severity of these issues, ventilated brake disks have been developed to enhance the heat dissipation capabilities of the rotor and decrease the likelihood of excessive disk temperatures from occurring [7]. Figure 2 compares the typical solid and ventilated brake rotor configurations available, i.e., solid, radial vane, and pin-finned.

Ventilated brake rotors essentially allow cooling air to flow into the core of the rotor and to move through its internal passages, thus enhancing the convective heat transfer of the rotor. The internal elements of the ventilated rotor, therefore, function like the vanes of a centrifugal impeller, which "pumps" cooling air through the core of the ventilated channels [1,8]. McPhee and Johnson [1] and Barigozzi et al. [9] further showed that the convective heat transfer (h_c) contribution of the internal passages is rotation speed dependent and has a significant effect on the overall

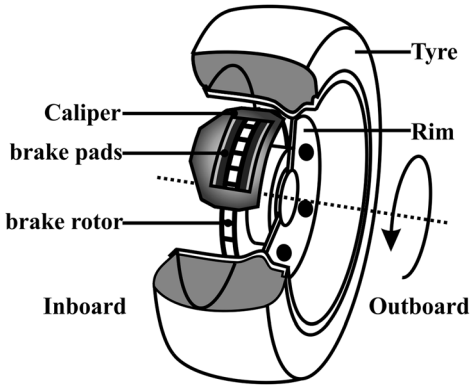

Fig. 1 Schematic of components of a typical brake system

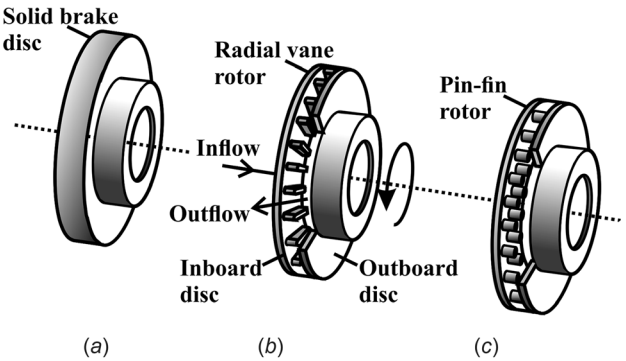

Fig. 2 Schematic of typical brake rotor configurations: (*a*) solid disk, (*b*) radial vane disk, and (*c*) pin-finned disk

[1]Corresponding author.

Contributed by the Heat Transfer Division of ASME for publication in the Journal of Heat Transfer. Manuscript received February 10, 2020; final manuscript received June 2, 2020; published online August 14, 2020. Editor: Portonovo S. Ayyaswamy.

convective cooling of the radial vane brake rotor: 45.5–55.4% for 342–1025 rpm and 50–70% for 750–1500 rpm.

The pin-finned rotor configuration is nowadays widely used in heavy vehicle braking systems as these rotors typically have a uniform distribution of mass throughout the rotor, resulting in a more even heat distribution in comparison to radial vane brake rotors [10,11]. This characteristic is desirable for heavy vehicle braking as it reduces the tendency of thermal distortion or cracking of the brake rotors [5,6,10,11]. The topology of a pin-finned brake rotor also increases the turbulence of the cooling flow passing through its internal passages. For example, Barigozzi et al. [12] revealed that the peak turbulence intensity measured at the brake rotor exit was ~1.53 times greater for the pin-finned rotor than the vane type. Lakshminarayana [13] reported that enhanced turbulence tends to augment convective heat transfer due to increased flow mixing and interaction of the cooling fluid and solid surfaces. Hence, the internal convective cooling (h_c) of a pin-fin rotor is governed primarily by flow mixing, which despite being less effective at pumping the cooling air, enables the rotor to achieve comparable cooling with the radial vane rotor (i.e., $h_{c,ave} = 36.2$ W/m^{2}K and 35.6 W/m^{2}K at 60 rad/s, respectively). Consequently, the cooling performance of the pin-fin rotor is better than the radial vane rotor at low rotation speeds, typical for heavy vehicle applications [10].

Despite the improved uniformity of the heat distribution as reported by Wallis [10], the measurements by Barigozzi et al. [12,14] revealed that both the turbulence and the time-averaged velocity distributions at the exit of pin-fin rotor passages are highly nonuniform. However, these authors did not investigate the local heat transfer distributions of the internal passages. On the other hand, Palmer et al. [15] conducted numerical simulations of unique pin-fin arrangements consisting of tear drop and diamond shaped elements, and reported a highly nonuniform heat transfer coefficient distribution over the internal surface of the outboard disk. Specifically, regions with high cooling flow velocity (high pressure side (P.S.)) relate to large heat transfer coefficients (~520 W/m^{2}K) and low velocity regions (trailing side) correspond to low heat transfer coefficients (~ 60 W/m^{2}K). That is, the internal surface of a pin-finned brake rotor exhibits significant variations of cooling. Further, the numerical results of Wallis et al. [11] showed that variations of cooling exist along the span of the pin fins, with the contribution of the inboard disk to the overall cooling of the internal passage being *less* than the average internal heat transfer. Although existing studies identified possible variations of cooling within the rotor passage (inboard versus outboard)), further explanation of this distinct heat transfer behavior remains elusive. In addition, Ramachandra et al. [4] reported that an asymmetric heating input to a solid brake rotor (i.e., variation of heat input to inboard and outboard disk surfaces) causes a temperature difference on the rotor surfaces, which in turn can lead to significant thermal stresses and distortion of the brake rotor (i.e., coning). As an asymmetric cooling distribution between inboard and outboard disks could also cause thermal distortion of the rotor, studying the internal cooling variations is of practical significance.

Based on the reviewed literature, there is a gap in the understanding of the local heat transfer distribution on the internal surfaces of pin-finned brake rotors. This is attributed mainly to the difficulty in experimentally accessing the internal regions of a rotating brake rotor where previous studies relied on either experimental measurements at the rotor exit or numerical simulations to gain insight into the internal cooling behavior within the brake rotor [14]. However, the correspondence of numerical heat transfer coefficient results with experimental measurements at the rotor exit is in general not good. For example, Barigozzi et al. [14] performed a comparative study of numerical and experimental heat transfer on a pin-finned rotor and presented results, which differ significantly, e.g., $h_{c,num} \approx 90$ W/m^{2}K versus $h_{c,exp} \approx 235$ W/m^{2}K. The large discrepancy was credited to experimental uncertainties and the possible limitations of numerical simulations (e.g., turbulence model) at accurately resolving the internal flow field within the pin-fin rotor. Thus, there is a need for further experimental results, which can not only provide additional physical insight into the local heat transfer distribution in pin-finned brake rotors (i.e., inboard and outboard surfaces) but also validate results obtained from future numerical simulations.

This study aims to experimentally map the local heat transfer distribution on the internal surfaces of a rotating pin-finned brake rotor so that an improved understanding of the local heat transfer variations on its inboard and outboard disk surfaces can be gained and the dependence of the internal surface heat transfer distributions upon rotation speed can be quantified. To this end, detailed internal surface temperature's variations within the rotating brake disk need to be mapped. Existing techniques of surface temperature mapping, such as the infrared (IR) thermography employed by Mew et al. [16] and Yan et al. [17], are considered to be unfeasible for this application, as the material making up the brake rotor are typically opaque to IR radiation, and hence the internal rotor surfaces would be experimentally inaccessible. Given these considerations, it is necessary to design an experimental method, which can overcome the difficulty in accessing the concealed internal regions of the rotor to facilitate the mapping of the internal local heat transfer. Such an experimental setup is presented in the current study. Specifically, a transient thermochromic liquid crystal method is adopted to obtain the internal convective heat transfer distributions by using instrumentation that is fixed onto the rotating brake disk. The proposed method enables detailed temperature maps of the internal surfaces to be *simultaneously* resolved at realistic rotation speeds for braking (e.g., $N = 100$–300 rpm).

Experimental Details

Test Setups and Instrumentation. The distribution of the convective heat transfer coefficient on the internal surfaces of a pin-finned brake rotor was measured using a custom-built test rig, as schematically shown in Fig. 3. The test rig consists of a brake rotor that rotates at varying yet controllable speeds and draws heated air from a heater chamber to facilitate transient heat transfer measurements. A bifurcated plenum together with a solenoid actuated spring-loaded flap enables rapid switching from the ambient air drawn into the rotor (i.e., flap closed) to the heated air that is stored in a heater chamber (i.e., flap open).

Thermochromic liquid crystal (TLC) was employed to map the distributions of local convective heat transfer coefficient (h_c) on the inner end-wall surfaces of the brake rotor by using the transient data reduction method [18–27]. A liquid crystal coating (i.e., Hallcrest R30C10W^{TM}) was applied to the inner end-wall surfaces (i.e., the inboard and outboard disks shown in Fig. 3), which undergoes a color change when exposed to temperature variations. The color change of the TLC was recorded in an red, green, blue color (RGB) scale video using a wireless camera (GoPro^{TM}), which was subsequently converted into the hue, saturation, intensity color (HSI) scale using MATLAB [28]. Based on in situ stationary calibration using T-type foil thermocouples (Omega^{TM}, Norwalk, CT), the surface temperature of the TLC coating was related to the video pixel hue value. The camera was mounted onto the rotating shaft supporting the brake rotor as shown in Fig. 3, and then focused on a fixed region of the brake rotor surfaces. The wireless function of the camera simplified subsequent data acquisition, as triggering of the camera was achieved remotely.

To facilitate internal surface temperature measurement using the TLC, a custom brake rotor was manufactured as shown in Fig. 4(*a*). The pin-finned rotor has transparent walls made from 10 mm thick acrylic (Perspex^{TM}) sheet, enabling optical access and, therefore, recording of TLC color change. Geometric parameters of the pin-fin rotor are shown in Fig. 4(*b*) while dimensions of the rotor are listed in Table 1, all based on an original equipment manufacturer brake rotor fitted to a commercial vehicle [16,17].

The experimental setup of Fig. 4 allowed the internal convective heat-transfer distribution of a rotating brake rotor to be determined by resolving the radial and circumferential variations

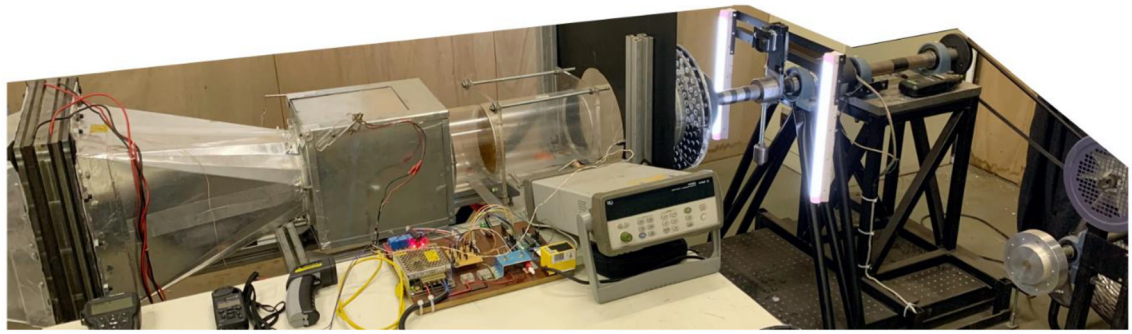

Fig. 3 Experimental setup using TLC to measure local heat transfer distribution in a rotating pin-finned brake rotor: (*a*) photograph and (*b*) schematic with detailed labels

of surface temperature in the *rotating reference frame*. To achieve this, the inner surface of the inboard disk was painted black using an airbrush and then the TLC was applied over the black backing paint layer. Similarly, as shown in Fig. 3, the outboard disk was coated first with the TLC and then the black backing paint was applied, which enhanced the reflectivity of the TLC coating, making its color change more distinct during video recordings. Figure 4(*a*) shows one half of the rotor painted with the TLC to monitor its color change on the inboard disk and the remaining portion of the rotor painted with the TLC on the outboard disk. To systematically compare the variations of convective heat transfer on the inboard and outboard inner surfaces, the rotor was orientated on the shaft so that the two coated surfaces were captured by the camera simultaneously, while experiencing the same thermal input from the heated air inflow. Therefore, the present transient method using the TLC and a transparent brake rotor enabled simultaneous measurement of convective heat transfer coefficient distributions on the inboard and outboard disk surfaces of the rotating pin-finned rotor.

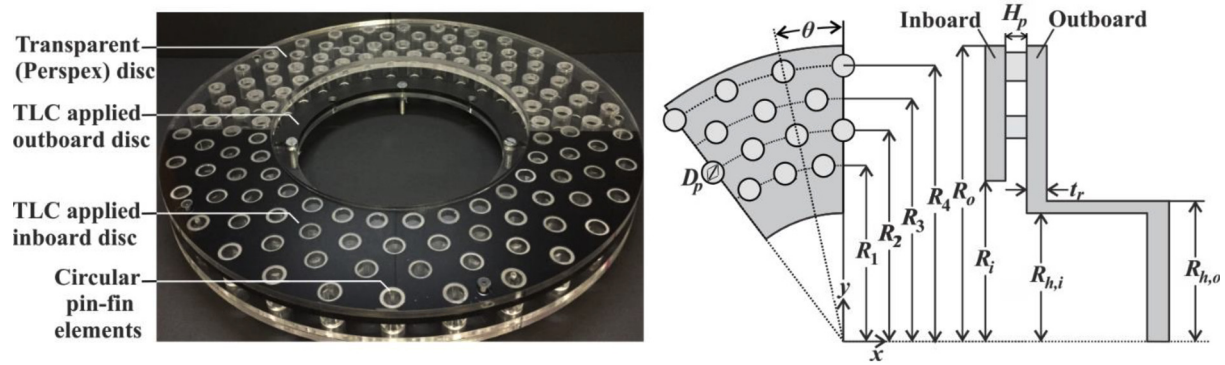

Fig. 4 A custom made transparent circular pin-fin brake rotor: (*a*) with TLC applied to inboard and outboard internal surfaces and (*b*) Schematic of geometric parameters

Table 1 Geometric and thermophysical parameters of pin-fin brake rotor

Parameter	Pin-fin rotor
D	336.0 mm
R_i, R_o	93.0 mm, 168.0 mm
D_p	13.0 mm
H_p	12.5 mm
t_r	10.0 mm
$R_{h,i}$, $R_{h,o}$	72.5 mm, 87.5 mm
$R_{1,2,3,4}$	102.5 mm, 121.5 mm, 139.0 mm, 157.0 mm
Θ	12.0 deg
Surface area density (ρ_{SA})	$\sim$198 m^2/m^3
Porosity (ε)	$\sim$0.74
$(\rho ck)^{1/2}$	556 $Ws^{1/2}/m^2K$

To quantify the pumping performance of the rotating pin-finned brake rotor, the mass flow rate ($\dot{m}$) was measured with a precalibrated rotating vane flowmeter (TSI LCA501) mounted into a circular plenum, the latter directing the airflow through the rotor core (Fig. 3). To prevent possible leakage flow, the plenum tube had a ring seal that was in contact with the rotor's external surface. The mass flow rate of the coolant stream drawn through the rotor's core was determined at varying angular speed (i.e., $N = 100$–300 rpm, corresponding to a heavy vehicle speed of 20–57 km/h). The brake disk was driven by a three phase induction motor that was controlled with a frequency inverter to precisely tune the motor speed, and the rotation speed (N) of the rotor was measured with a digital tachometer.

Data Reduction. Based on the solution to the one-dimensional (1D) Fourier conduction equation, i.e., Eq. (1), the transient technique determines the local heat transfer coefficient (h_c) for each pixel during video recording. The boundary conditions for this equation assume a semi-infinite solid and convective heat transfer between the heated air flow and the solid (i.e., the acrylic internal surface of the rotor). The semi-infinite solid assumption requires that the acrylic disk walls are sufficiently thick to ensure that the far-side (external) wall temperature remains constant during the process of transient heating [29]

$$\frac{\partial T}{\partial t} = \alpha \frac{\partial^2 T}{\partial z^2} \tag{1}$$

Based on the above assumptions and an ideal step function increase of gas temperature (T_g), the solution to Eq. (1) is obtained by Laplace transform [30,31], as

$$\frac{T_s - T_0}{T_g - T_0} = 1 - \exp\left(h_c\sqrt{\frac{t}{\rho ck}}\right)^2 \operatorname{erfc}\left(h_c\sqrt{\frac{t}{\rho ck}}\right) \tag{2}$$

The initial condition is that, at $t = 0$, the solid is at uniform temperature (T_0). Thereafter, the surface temperature of the solid (T_s), as determined by the calibrated TLC color change, increases in response to the step increase of gas temperature. The convective heat transfer coefficient (h_c) relates to the heat transfer between the flow and the solid and is assumed constant during the entire transient process [22,24].

In reality, most transient heat transfer experiments are unable to generate the idealized step increase of driving gas temperature. Instead of Eq. (2), Gillespie et al. [20] derived an alternative solution

$$\frac{T_s - T_0}{T_g - T_0} = 1 - \frac{\rho ck/h_c^2\tau}{1 + (\rho ck/h_c^2\tau)}\exp\left(h_c\sqrt{\frac{t}{\rho ck}}\right)^2 \operatorname{erfc}\left(h_c\sqrt{\frac{t}{\rho ck}}\right) \ldots - \exp(-t/\tau) \times \frac{1}{1 + (\rho ck/h_c^2\tau)}\left\{1 + \frac{\sqrt{\rho ck}}{h\sqrt{\tau}} \times \left[\frac{1}{\pi}\left(\frac{t}{\tau}\right)^{1/2} + \frac{2}{\pi}\sum_{n=1}^{\infty}\frac{1}{n}\exp(-n^2/4)\sinh\left[n\left(\frac{t}{\tau}\right)^{1/2}\right]\right]\right\} \tag{3}$$

by employing an exponential gas temperature rise boundary condition

$$T_g(t) = T_0 + (T_{g,\infty} - T_0)(1 - \exp(-t/\tau)) \tag{4}$$

Here, $T_{g,\infty}$ is the asymptotic gas temperature, τ is the time constant of the gas temperature ($T_g(t)$), $(\rho ck)^{1/2}$ is the thermal product, and erfc (…) is the complementary error function. Local convective heat transfer coefficient (h_c) at discrete pixel locations is determined via a nonlinear least squares regression. Note that h_c is the value that provides the best fit with the calculated temperatures from Eq. (3), the measured TLC surface temperature ($T_s(t)$) and the gas temperature ($T_g(t)$) histories. The duration of the discrete pixel sampling from ($t = 0$) was determined by two criteria: (1) the thermal pulse created by the gas temperature rise cannot cause the external rotor surface temperature to increase by more than 1%—*penetration time* [24,29,32], and (2) the maximum hue value (i.e., $\text{hue}_{\max} < 0.64$) based on in situ calibration cannot be exceeded, which defines the overall TLC indication time (t_1) for each pixel.

The transient method requires rapid heating of the airflow. Gillespie et al. [20] designed an air heating system to generate a rapid exponential rise (Eq. (4)) of gas temperature (i.e., time constant (τ) < 1.4 s) so that the driving gas temperature rise is a close approximation to the ideal step function. The heating system used a densely packed heating mesh to uniformly heat the inflow, yet strong fans are also required to overcome the pressure drop created by the fine-wire heating mesh (i.e., wire diameter $\sim$40 μm and mesh porosity $\varepsilon_{\text{heater}} = 0.38$). On the other hand, the present experimental setup relies on airflow *induced* by the rotating brake rotor. Therefore, the air heating system implemented by Gillespie et al. [20] would adversely affect the pumping performance of the pin-finned brake rotor and potentially alter the internal flow and heat transfer behavior. To balance these conflicting requirements, the air heater shown in Fig. 3 utilized a highly porous ($\varepsilon_{\text{heater}} \approx 0.97$) heater mesh made from 0.45 mm diameter Nichrome (NiCr80) resistance wire, to minimize the pressure drop across the heater and, therefore, not affect the rotor pumping performance (to be validated experimentally). Rapid air heating was achieved by heating the air in a large volume chamber until thermal equilibrium was reached, and then triggering a thermal pulse by rapidly switching the inflow air source from the ambient to the heated air trapped within the heater chamber. Due to the reliance of the air heater on the pumping of air by the brake rotor, there is a coupling of the temporal variation of gas temperature to rotor pumping performance, which leads to the gas temperature time constant (τ) being dependent on rotor rotation speed (N). Despite the gas temperature ($T_g(t)$) being accurately modeled by (Eq. (4)) for various rotation speeds considered (i.e., $N = 100$–300 rpm), preliminary investigations revealed that Gillespie's solution (Eq. (3)) tended to overestimate the local heat transfer coefficient (h_c) when the TLC indication time (t_1) was comparable to the time constant (τ) (i.e., $\tau > 0.2t_1$). The resulting time constants in the present experimental setup are long (i.e., $\tau = 6.6$–25.0 s) in comparison with previous TLC studies of Gillespie et al. [20] and Kim et al. [33] where the time constants were short (i.e., $\tau < 1.4$ s). Thus, the maximum hue value (i.e., $\text{hue}_{\max} = 0.64$) of a pixel was sometimes obtained before an asymptotic gas temperature ($T_{g,\infty}$) could be established, e.g., in regions with high convective heat transfer coefficients.

The overestimated heat transfer coefficients by Gillespie's solution in the present setting were resolved by applying Duhamel's principal of superposition to Eq. (2) to provide a solution to local convective heat transfer coefficient (h_c) [18,19,23,26,27,34,35], particularly when the gas temperature profile was *nonasymptotic*, as

$$T_s - T_0 = \sum_{j=1}^{N}\left[1 - \exp\left(h_c\sqrt{\frac{t_1 - \tau_j}{\rho ck}}\right)^2 \operatorname{erfc}\left(h_c\sqrt{\frac{t_1 - \tau_j}{\rho ck}}\right)\right]\Delta T_{g(j,j-1)} \tag{5}$$

Equation (5) calculates the overall increase of surface temperature ($T_s - T_0$) at discrete pixel locations over the duration of TLC indication time (t_1). A series of finite surface temperature steps were calculated based on delayed time steps defined by the TLC indication time (t_1, which is *constant* inside the summation), the dummy time variable (τ_j, which approaches t_1 with increasing index variable j), and the gas temperature steps ($\Delta T_{g(j,j-1)}$). The convective heat transfer coefficient (h_c) in Eq. (5) was determined using the Newton–Raphson method, which converged rapidly with ($k = 8$) iterations, as

$$h_{c,k+1} = h_{c,k} - F(h_{c,k})/F'(h_{c,k}) \tag{6}$$

The gas temperature was measured with 5 T-type bead thermocouples (Omega) circumferentially placed at both the inlet and exit of the brake rotor (10 thermocouples in total) at 45 deg increments (Fig. 3). The time-dependent gas temperature was defined according to the spatially averaged inlet and exit gas temperatures from the thermocouples. Temporal variation of gas temperature was recorded by a multichannel data acquisition unit (Agilent™ 34972 A) where the triggering was synchronized with the switching on of light emitting diode (LED) illumination when a transient test was initiated. It was observed that the gas temperature varied within the rotor passage where the gas temperature between the rotor inlet and exit decreased. Hence, when solving the semi-infinite conduction equation (Eq. (5)) at each pixel, the local driving gas temperature (T_g) was interpolated as a linear function of radial position (R) based on the temporal variation of average inlet and exit gas temperatures.

Heater Performance and Thermochromic Liquid Crystal Calibration. This study aims to improve the understanding of local heat transfer distributions within pin-finned brake rotors. To this end, the transient method adopted requires the pin-finned rotor to pump heated air from the heater chamber (Fig. 3), without reducing its pumping performance. Consequently, the heater system utilizes a highly porous heater mesh to minimize the restriction to air flow. Figure 5(*a*) compares the pumping performance of the pin-fin brake rotor with and without the heater mesh to quantify the influence of the inserted mesh heater on mass flow rate ($\dot{m}$) for selected rotation speeds (N). It is shown that the heater mesh does not have any significant influence on pumping performance for the range of rotation speeds tested. For both test configurations, there is a linear variation of mass flow rate with rotation speed. It is, therefore, assumed that the present heat transfer setup has an insignificant effect on the internal flow behavior of pin-finned rotors.

Since the driving gas temperature for the present transient heat transfer tests is supplied by the rotating pin-finned rotor, its variations are effectively coupled with the pumping capacity of the rotor. Figure 5(*b*) shows the monotonic relationship between the time constant (τ) with rotation speed (N). The time constant was determined by least square regression to achieve best fit using Eq. (4) and the measured average inlet temperature. The transient heat transfer tests, therefore, have steady-state fluidic boundary conditions due to constant rotation speed and mass flow rate. However, the thermal boundary conditions are unsteady, for the convective heat transfer measurements are initiated by an exponential gas temperature rise. Hence, during a transient test, it is rather the steady fluidic condition that governs the convective heat transfer coefficient and forms the basis for assuming a constant local heat transfer coefficient (h_c) during the transient process.

As the transient method determines the heat transfer coefficient based on the temporal response of surface temperatures, in situ calibration was performed so that a systematic comparison of the inboard and outboard heat transfer behaviors could be made. Two T-type foil thermocouples were bonded to the TLC coating of the inboard and outboard surfaces to minimize the obstruction to the airflow, as shown in Fig. 6(*a*). A centrifugal fan was used to drive the air through the heater mesh and the *stationary* rotor passages, at a mass flow rate equivalent to when the rotor was rotating at $N = 300$ rpm (Fig. 5(*a*)). Stationary calibrations were then carried out by gradually increasing the air heater power to raise the temperature of the air passing through the rotor passages. As the increased gas temperature initiates the TLC color change, the visible spectrum of the TLC was recorded, initially from black (background) to black (background) via Red→Green→Blue as exemplified in Fig. 6(*a*). Small subregions of 10×10 pixels adjacent to the junction of the foil thermocouples were extracted from the video recordings and spatially averaged to obtain average RGB scale values. The RGB value was then converted into the HSI scale where only the average hue values were related to the measured temperatures recorded simultaneously with the data acquisition unit. Figure 6(*b*) presents calibration curves that correlate average hue values to TLC temperatures using a third order polynomial fit, as

$$T_{s,\text{in}} = 57.532\text{hue}^3 + 6.0555\text{hue}^2 - 7.6773\text{hue} + 32.97 \tag{7}$$

$$T_{s,\text{out}} = -224.65\text{hue}^3 + 385.26\text{hue}^2 - 166.61\text{hue} + 54.65 \tag{8}$$

This method of calibration ensures that identical LED illumination and camera settings could be maintained for both the calibration and the rotating transient heat transfer tests. This facilitated

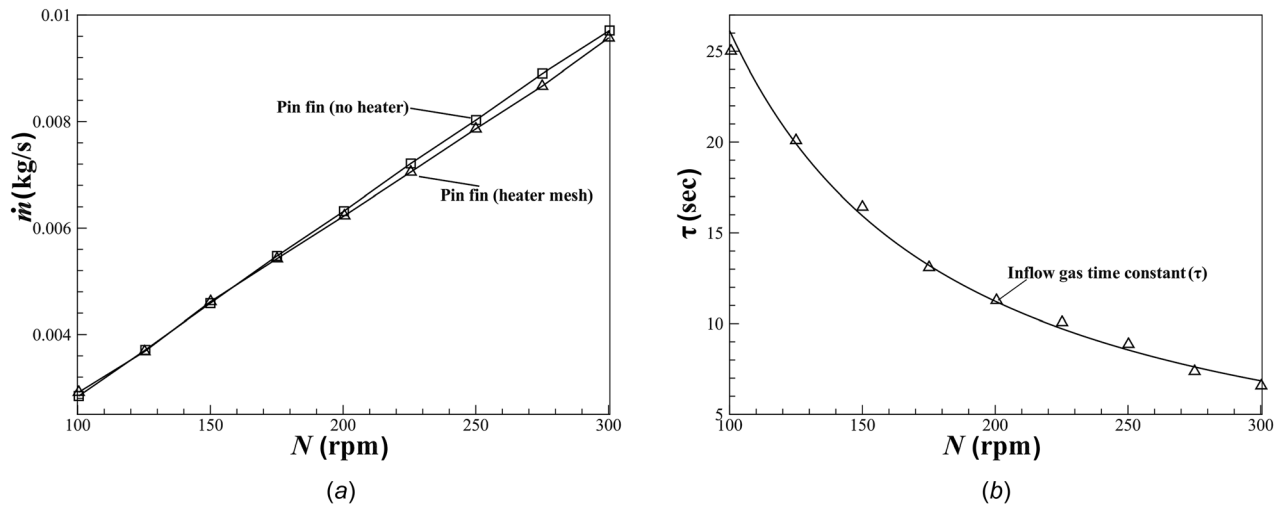

Fig. 5 Performance of air heater system, which is dependent on the pumping capacity of pin-finned rotor: (*a*) mass flow rate ($\dot{m}$) varying with rotation speed (N) and (*b*) Inflow gas time-constant (τ) varying with rotation speed (N)

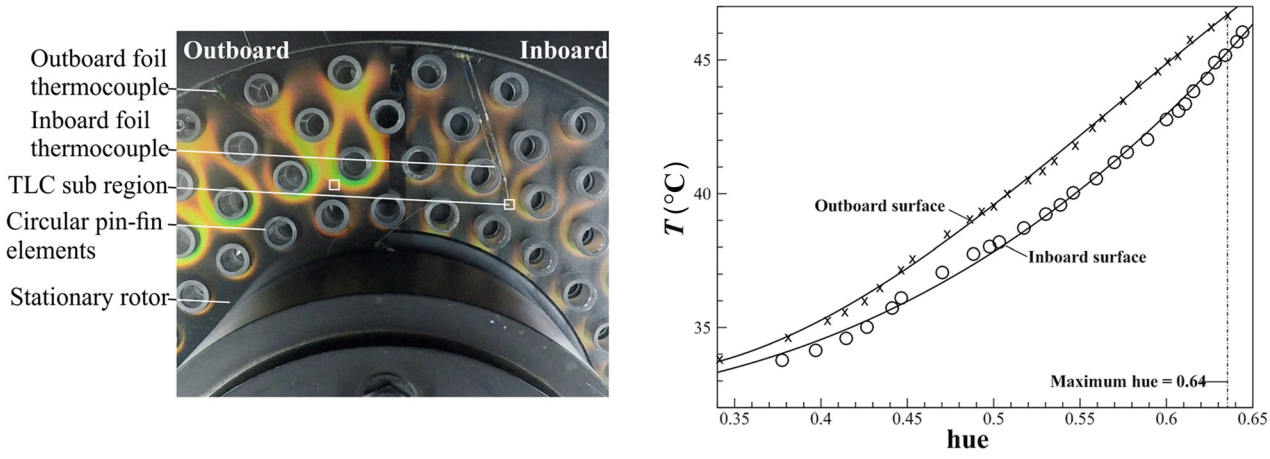

Fig. 6 Simultaneous in situ TLC calibration of inboard and outboard surfaces with a stationary rotor: (*a*) image from raw TLC video where RGB color data are extracted from TLC subregions and (*b*) calibration curves of TLC temperature with hue value

Table 2 Experimental uncertainty of local heat transfer coefficient (h_c)

Uncertainty source (Δ)	Low local heat transfer ($h_c = 8.0$ W/m^{2}K)		High local heat transfer ($h_c = 350.2$ W/m^{2}K)	
		Relative uncertainty of h_c		Relative uncertainty of h_c
Gas temperature (ΔT_g)	± 0.1 °C	3.04 %	± 0.1 °C	4.56%
TLC temperature (ΔT_s)	± 0.24 °C	10.9 %	± 0.24 °C	4.95%
Initial temperature (ΔT_0)	± 0.24 °C	10.6 %	± 0.24 °C	4.67%
TLC indication time (Δt_1)	± 0.0015 sec	0.002%	± 0.0015 sec	0.32%
Thermal product ($\Delta_{\sqrt{}}\rho ck$)	± 14 Ws$^{1/2}$ /m^{2}K	0.03%	± 14 Ws$^{1/2}$ /m^{2}K	0.03%
Overall uncertainty in local heat transfer (U_h)—RSS		15.5%		8.2%
Spatially averaged relative uncertainty ($U_{h,\text{ave}}$)		9.0%		Outboard side ($N = 300$ rpm)

systematic comparison of the local heat transfer coefficient variations between the inboard and outboard surfaces at different rotation speeds.

Measurement Uncertainties. The local convective heat transfer coefficient (h_c) is a function of the following measured variables: the driving gas temperature (T_g), the TLC surface temperature (T_s), the initial temperature (T_0), the thermal product ($(\rho ck)^{1/2}$) of the rotor material, and the TLC indication time (t_1). Thus, the experimental uncertainty of the local heat transfer coefficient, U_h, is related to the uncertainties inherent in the measured variables, which are propagated in the primary data reduction equation (Eq. (5)). The overall uncertainty for each of the measured input variables typically consists of the root-sum-square (RSS) contribution of the systematic and random uncertainties [36]. However, only random uncertainties were estimated as careful calibration of the input variables has been undertaken to minimize the contribution of systematic uncertainties. Thus, the random uncertainties for all the input parameters are summarized in Table 2, based on 20 to 1 odds.

Overall uncertainty in the local heat transfer coefficient was estimated using the method of *sequential perturbations* that is well suited to computerized uncertainty analysis [37–39]. The primary advantage is that the need to perform direct differentiation of the data reduction equation (Eq. (5)) is removed, which is convenient due to the implicit form of Eq. (5). Finite difference approximations of the data reduction equation are estimated by sequentially perturbing the input variables ($\pm\Delta$) and then solving Eq. (5) repeatedly to determine the sensitivity of heat transfer to various perturbations. The overall uncertainty is then estimated by taking the RSS of the contributing terms shown in Table 2. The relative uncertainty is determined to be $U_h \approx 8.2\%$ for the high heat transfer region and $U_h \approx 15.5\%$ for the low heat transfer region, comparable to the uncertainty estimates of Gillespie [39] (i.e., $U_h \approx 7.7$–14.0%) and Steurer et al. [27] (i.e., $U_h < 11.2\%$). For instance, the spatially averaged overall uncertainty for the sampled outboard surface is $U_r \approx 9.0\%$ at $N = 300$ rpm. The uncertainty of the bulk velocity measurement from the flowmeter was ± 0.02 m/s and the digital tachometer had an accuracy of 0.05%.

Results and Discussion

Mapping the Internal Surface Temperatures. Figure 7 exhibits the internal TLC color map of the outboard disk at constant rotation speed (i.e., $N = 300$ rpm), representative of the braking conditions for heavy vehicles traveling at 57 km/h. In view of the temporal color change of the TLC coating at $t = 0.0$ s, most of the outboard surface is "green." The effect of heated gas inside the vented passages is observed in Fig. 7(*b*) at $t = 7.0$ s. A change of color begins from the first row of pin fins (i.e., green to blue). Farther away from the rotor hub and closer to the exit, the initial color remains unchanged (i.e., green), particularly in distinct regions aft of the circular pin fins. The color (i.e., temperature) maps display strong periodicity, with the blue color regions following a regular and repeating pattern on the rotor surface, which is indicative of an even distribution of flow across each rotor passage.

The blue patterns follow inline backward sweeping paths that are curved in the opposite direction to the rotor rotation. It is apparent in Fig. 7(*c*) that the majority of the outboard rotor surface is "blue," so in general when there is a gas temperature rise, the surface temperature increases, progressively moving outward with time. This color map behavior is observed for all the rotation speeds tested (i.e., $N = 100$–300), suggesting that the flow pattern is largely independent of rotation speed. However, the rate of

Fig. 7 Raw RGB images of internal surface temperature distributions on the outboard surface of pin-finned rotor at $N = 300$ rpm: (*a*) $t = 0$ s, (*b*) $t = 7.0$ s, and (*c*) $t = 34.6$ s

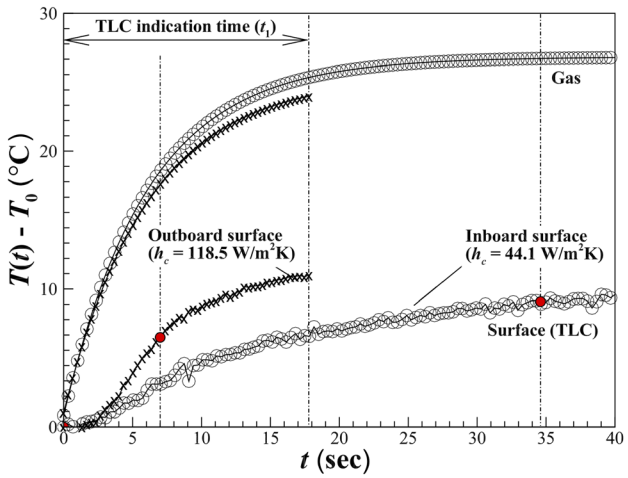

Fig. 8 Driving gas temperature and TLC surface temperature plotted as functions of time for inboard and outboard surfaces, extracted from a pixel location (i.e., red dot) in Fig. 7, at $N = 300$ rpm

color (i.e., temperature) change decreased substantially for relatively low rotation speed, requiring longer recording times for these transient tests.

Figure 8 shows a typical gas and surface temperature variation with time, extracted from a fixed location (i.e., "red dot") in Figs. 7(*a*)–7(*c*). Here, a specific pixel has been sampled and the variation of hue with respect to time has been converted into the measured surface temperature ($T_s(t)$) by Eqs. (7) and (8). The increase of surface temperature from an initial temperature (T_0) is in response to the exponential rise of gas temperature ($T_g(t)$). A comparison between the surface temperature responses of the inboard and outboard surfaces at equivalent pixel locations highlights the differences in heat transfer between the two surfaces. The outboard surface reveals that it takes a significantly shorter period of time to reach the temperature corresponding to the maximum hue value (see Fig. 6(*b*)). The rapid increase of surface temperature is indicative of a high local heat transfer coefficient (i.e., $h_c = 118.5$ W/m^{2}K). In addition, the time constant (i.e., $\tau \approx 6.6$ s) is comparable to the TLC indication time ($t_1 \approx 17.7$ s and $\tau/t_1 \approx 0.37$)), so that the exponential driving gas temperature could not reach the asymptotic temperature ($T_{g,\infty}$). In such instances, it is observed that Gillespie's equation (Eq. (3)) overestimates the heat transfer coefficient (i.e., $h_c = 160.4$ W/m^{2}K) and, therefore, Duhamel's principle (Eq. (5)) is used for subsequent heat transfer coefficient calculations.

On the other hand, the inboard surface requires a significantly longer period of time for its temperature to increase. The low calculated heat transfer coefficient (i.e., $h_c = 44.1$ W/m^{2}K), therefore, indicates that the inboard surface has less heat transfer than the outboard surface. Furthermore, the gas temperature reaches an asymptotic state and consequently the calculated (i.e., $h_c = 45.1$ W/m^{2}K) values using Gillespie's equation (Eq. (3)) are a close match to those calculated using Duhamel's principle (Eq. (5)).

Figures 9(*a*) and 9(*b*) present local heat transfer distributions on the inboard and outboard surfaces of the pin-finned rotor, respectively, at a fixed rotation speed (i.e., $N = 300$ rpm). The results demonstrate a large difference of heat transfer behavior between the two internal surfaces. On the inboard surface (Fig. 9(*a*)), local heat transfer is evenly distributed along radial and circumferential directions at the outermost regions of the rotor passages, but is highly nonuniform at the entrance region, with reduced heat transfer. In contrast, on the outboard surface (Fig. 9(*b*)), the innermost region (near the hub) has the greatest heat transfer, where the bulk of air flow is concentrated in the narrow gaps between the first and second rows of pin fins. The magnitude of heat transfer then decreases upon moving radially outward, but also becomes more evenly distributed in the radial and circumferential directions. On both surfaces, there are also distinct regions with significantly lower heat transfer coefficients (i.e., the suction side (S.S.)) than the mainstream flow regions, which also resemble the wake regions that develop when a bluff body is immersed in a uniform air stream [40]. Figure 9 also reveals that the inboard surface has significantly lower heat transfer capabilities than the outboard rotor, suggesting that there are large thermal gradients that develop within the pin fins, which may result in thermal stresses and distortion of the brake rotor (i.e., coning).

Figure 10 compares the circumferential distributions of local heat transfer coefficient ($h_c(S)$) on the inboard and outboard surfaces at selected radial locations (i.e., R_1 to R_4), corresponding to the first to fourth rows of pin fins in Fig. 9. Figure 10(*a*) exhibits that the outboard rotor obtains high heat transfer coefficient values (i.e., $h_c \approx 350$ W/m^{2}K) within the first row. From Fig. 9(*b*), these high heat transfer regions can be seen to occur on the leading face of the pin fins, i.e., the P.S. At the entrance, the inflow encounters the minimum flow area at the first row of pin fins, which causes the inflow to accelerate and hence increases the local shear stress (skin friction). In addition, as the bulk flow impinges on the pin fins, horse-shoe vortex structures may also develop as described in Kim et al. [33]. The combination of increased local skin friction and horse-shoe vortex formation may account for the high local heat transfer observed in the gap of the first pin-fin row. Adjacent to the peak is the substantially low local heat transfer value (i.e., $h_c \approx 43.0$ W/m^{2}K), which is associated with the trailing side of the pin fins, i.e., the S.S. This low heat transfer can be attributed to the establishment of separated wake flow that inhibits the

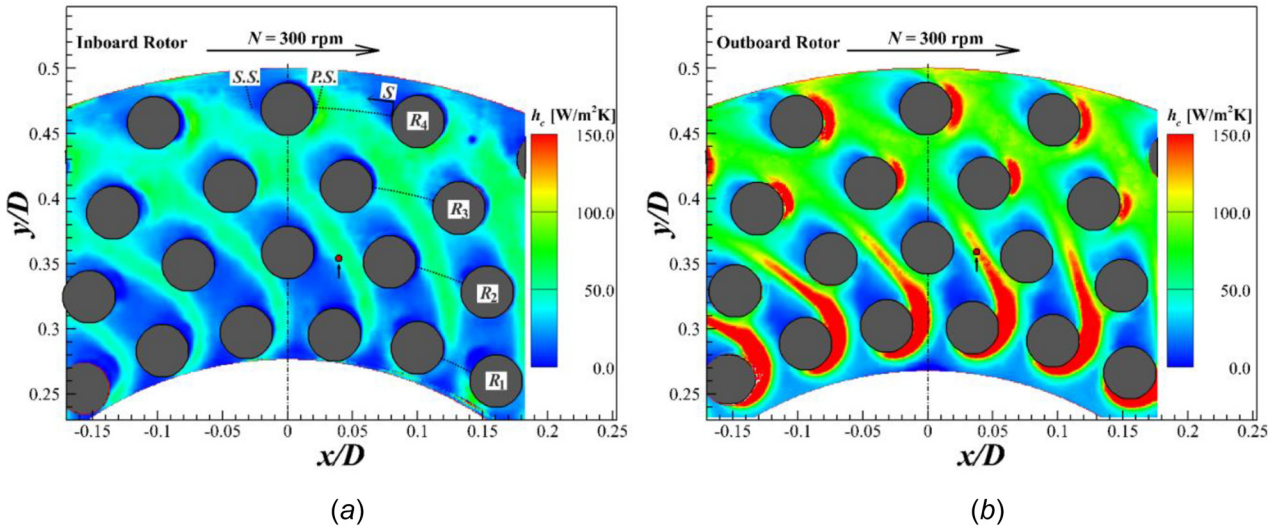

Fig. 9 Radial and circumferential variations of local heat transfer coefficient (h_c) on (*a*) inboard surface and (*b*) outboard surface of pin-finned rotor where the P.S. and S.S. of the pin fins are shown.

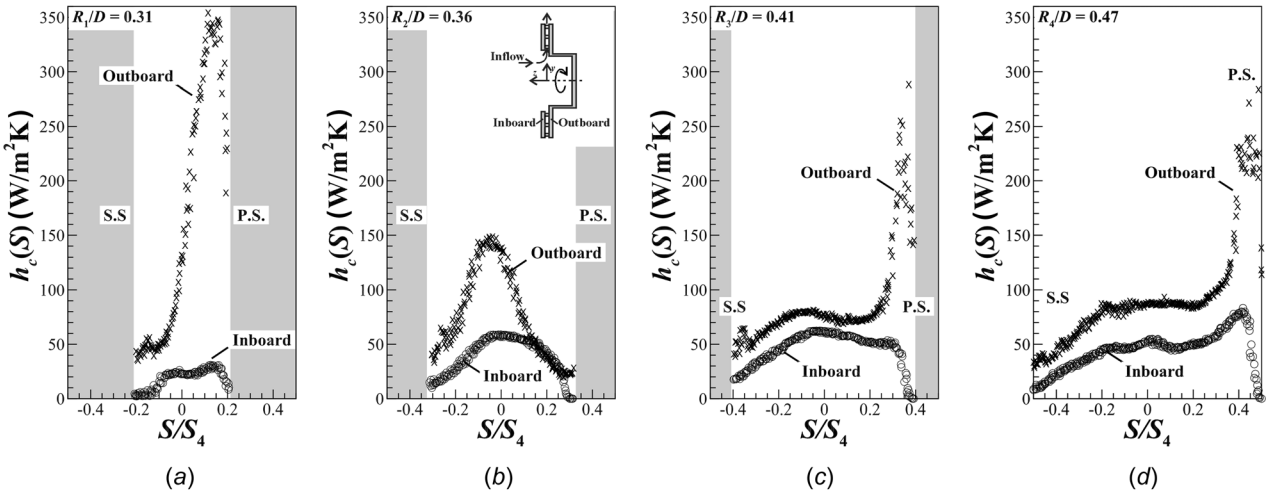

Fig. 10 Variation of heat transfer coefficient (h_c) in circumferential direction (S) for pin-fin rows extracted from Fig. 9: (*a*) first row of pin fins (i.e., $R_1/D = 0.31$), (*b*) second row of pin fins (i.e., $R_2/D = 0.36$), (*c*) third row of pin fins (i.e., $R_3/D = 0.41$), and (*d*) fourth row of pin fins (i.e., $R_4/D = 0.47$)

replenishment of air into the suction side region, thus reducing the local convective heat transfer coefficient. Consequently, large thermal gradients develop in the passages adjacent to the pressure and suction side regions.

The inboard local heat transfer coefficients associated with the first row are more evenly distributed than the outboard surface, yet are also significantly lower in magnitude. This difference is possibly related to how the inflow behaves at the entrance to the rotor passage, where an abrupt change in geometry occurs, causing the air to change suddenly from the axial (i.e., z-axis) to radial direction, as illustrated by the inset of Fig. 10(*b*). This disruption may then force the inflow adjacent to the inboard surface to become separated, with a recirculation zone forming on the surface. The formation of the recirculating zone then reduces local heat transfer. The results of Fig. 10(*b*) reveal that the size of the recirculation zone is possibly midway between the first and second rows, as heat transfer on the inboard surface increases at the second row. As for the outboard surface, the reduced heat transfer at the second pin-fin row could be related to the decreasing strength of the horse-shoe vortex structures on the P.S. of the pin fins.

On the other hand, Figs. 10(*c*) and 10(*d*) for the third and fourth pin-fin rows indicate that the inboard surface has increased peak heat transfer in comparison to the second row, which could be attributed to the re-attachment of bulk airflow to the inboard surface. There is also the formation of a "plateau" between the pressure and suction side faces of the pin fins, corresponding to convective heat transfer due to the bulk airflow. The severity of the thermal gradients has decreased, so in general the local heat transfer is more uniformly distributed at the outer most regions of the brake rotor.

Similarly, for passages in the third and fourth pin-fin rows on the outboard surface, the circumferential variation of heat transfer can be categorized into three distinct regions, as follows.

(1) There is a sharp peak, which has similar characteristics as the local heat transfer distribution related to horse-shoe vortex structures forming on the P.S. of pin fins. The slight reduction of peak heat transfer value (i.e., $h_c \approx 257$ W/m^{2}K) in comparison to the first row (i.e., $h_c \approx 350$ W/m^{2}K) is possibly related to the decreased fluid momentum that is caused when the passage's effective flow area increases as the flow follows its backward curving path.
(2) In the mid region between the pin fins, a "plateau" forms where the local heat transfer is quite constant, which can therefore be attributed to bulk airflow movement.

(3) A minimum of local heat transfer is observed, relating to the S.S. of the pin fins, which has a reduced heat transfer coefficient caused by separated flow occurring on the trailing side of pin fins.

Figure 11 shows the variation of heat transfer coefficient averaged along the circumferential direction for each row, which provides further insight of the airflow behavior underpinning the heat transfer distribution within the rotor. Upon comparing the inboard and outboard surfaces on a row by row basis, the first row average heat transfer for the outboard side is large (i.e., $h_c \approx 165$ W/m^{2}K). This causes the greatest variation of heat transfer in the z-axis (coinciding with the axis of the brake rotor), as the inboard surface heat transfer is very low (i.e., $h_c \approx 19$ W/m^{2}K). The significant variation is related to the inflow transitioning abruptly from the z-axis to the y-axis (coinciding with the radial direction), which creates an inboard side recirculation zone by the first pin-fin row that causes the observed low heat transfer. On the other hand, the airflow adjacent to the outboard surface is attached and, therefore, can enhance the local heat transfer.

From the second pin-fin row, the average heat transfer increases slightly, despite the decreased local fluid momentum in the outermost regions of the passage. The increasing heat transfer at the third and fourth rows, therefore, suggests that the bulk flow turbulence investigated by Barigozzi et al. [12] is a significant factor, which further augments heat transfer in the outermost regions even when the average fluid momentum is decreasing due the increasing bulk flow area (Fig. 7).

Inboard and Outboard Heat Transfer Varying With Rotation Speed. The present experimental setup facilitates transient surface temperature mapping on the inboard and outboard surfaces simultaneously, thus enabling spatially averaged convective heat transfer coefficients to be calculated over a range of rotation speeds. Figure 12 shows that the outboard surface has approximately twice the average heat transfer coefficient over the inboard surface (i.e., $h_{c,\text{ave,out}} \approx 2\,h_{c,\text{ave,in}}$) for the internal disk surfaces (excluding those occupied by pin fins). It also appears that in this narrow operating range, the averaged heat transfer on both surfaces increases linearly with rotation speed although it is expected that, at substantially higher rotating speeds, the averaged heat transfer on each surface might approach an asymptotic value as thermal saturation takes place.

In summary, the averaged heat transfer coefficients for the inboard and outboard surfaces differ significantly from the averaged heat transfer of the passage (i.e., inboard + outboard), which illustrates the possibility of large thermal gradients existing along

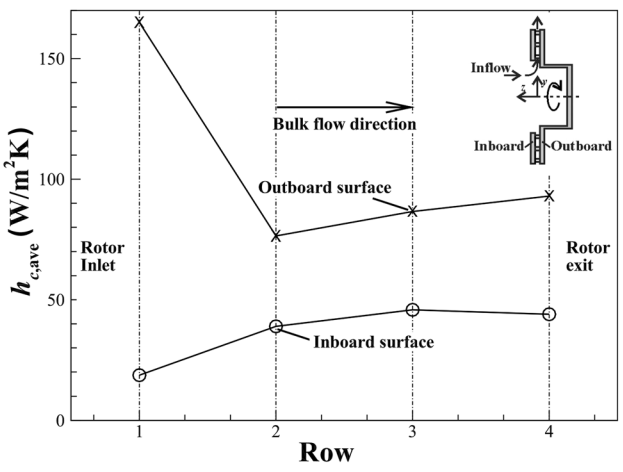

Fig. 11 Variation of circumferentially averaged heat transfer coefficient (h_c) for different rows of pin fins along rotor passages, based on Fig. 10 where $N = 300$ rpm

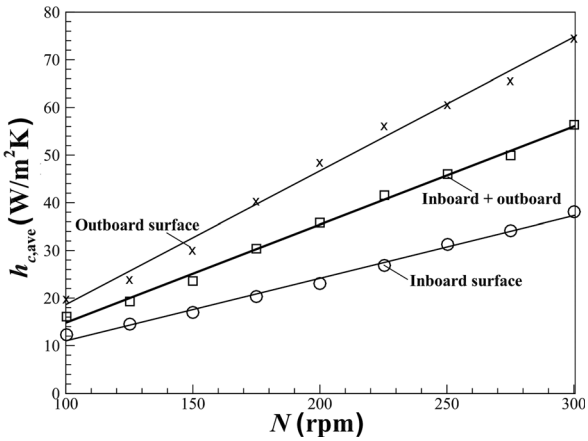

Fig. 12 Spatially averaged heat transfer coefficient ($h_{c,ave}$) plotted as a function of rotation speeds (N) for inboard, outboard and combined surfaces

the span of pin fins. Ramachandra et al. [4] reported that unequal thermal inputs into a brake rotor can lead to substantial temperature differences, therefore inducing large thermal stresses that exacerbate thermal distortion of the rotor. The asymmetric distributions of convective heat transfer coefficient on the inboard and outboard surfaces are analogous to the unequal thermal inputs reported by Ramachandra et al. [4]. Hence, it is plausible that large variations of local heat transfer coefficient may too exacerbated thermal distortion of the pin-finned rotors.

The simplified experimental setup where the brake disk is rotating in *quiescent* air is not expected to greatly alter the local internal heat transfer behavior in comparison to a pin-finned brake rotor fitted to a heavy vehicle on the road. The adverse flow disturbance caused from the caliper, wheel, and the wheel house, as well as cross-flow due to the vehicle's motion have been excluded in this study. However, Stephens et al. [41] have demonstrated that an airflow test of a brake rotor in still air yielded similar flow behavior at the exit of the brake rotor as the one obstructed by a wheel and wheel house with cross-flow, which suggests that the internal flow behavior may not be substantially affected by the external airflow disturbances. The present spatially averaged internal heat transfer coefficient is also comparable to the values reported by McPhee and Johnson [1], who conducted bulk internal convective heat transfer measurements using a cast iron radial vane rotor at representative vehicle brake disk operating temperatures (i.e., 856 °C). For similar low rotation speeds (i.e., $N = 342$ rpm), their average internal convective heat transfer (i.e., $h_{c,\text{ave}} \approx 27$ W/m^{2}K) is within an order of magnitude of this study (i.e., $h_{c,\text{ave}} \approx 56$ W/m^{2}K), where the discrepancies are possibly attributed to the vastly different rotor geometries (i.e., radial vanes versus pin-finned brake rotor) and conduction and radiative heat losses through the rotor hub. Thus, employing a custom made transparent acrylic brake rotor for the transient TLC heat transfer measurements yields local internal heat transfer distributions that are largely representative of the cooling behavior within a pin-finned brake rotor fitted on a heavy vehicle.

Conclusions

This study examined local heat transfer coefficient distributions obtained experimentally on the interior surfaces of a rotating pin-finned brake rotor at realistic rotation speeds for heavy vehicle braking (i.e., $N = 100$–300 rpm). The transient thermal mapping method using thermochromic liquid crystals in a rotating reference frame was employed. Main findings are as follows:

(a) The bulk airflow within the ventilated channel of a rotating disk follows a predominantly backward sweeping inline-

like path between the pin fins, despite the pin fins having a staggered arrangement when observed in a stationery reference frame.

(b) Internal local heat transfer is distributed nonuniformly on both the inboard and outboard surfaces of the pin-finned rotor. The extent of local thermal nonuniformity on the outboard surface is substantial in comparison to the inboard surface.

(c) The outboard surface has twice the average cooling of the inboard surface, which possibly exacerbates thermal stresses in both surfaces.

(d) Thus, there might be a large thermal gradient along the span of pin fins, causing thermal distortion of the rotor (i.e., coning).

Nomenclature

c = solid material thermal capacity (J/kgK)
D = rotor diameter (m)
h_c = convective heat transfer coefficient (W/m^{2}K)
$h_{c,\mathrm{ave,in}}$ = averaged convective heat transfer coefficient on inboard surface (W/m^{2}K)
$h_{\mathrm{c,ave,out}}$ = averaged convective heat transfer coefficient on outboard surface (W/m^{2}K)
HSI = hue, saturation, intensity color scale
j = index parameter
k = solid material thermal conductivity (W/mK)
$\dot{m}$ = mass flow rate (kg/s)
N = rotation speed (rpm)
R = radial position (m)
RGB = red, green, blue color scale
rpm = revolution per minute
S = normalized distance parameter (m)
t = time (s)
t_r = thickness of both inboard and outboard disks (m)
t_l = TLC indication time (s)
T_g = gas temperature (°C)
$T_{g,\infty}$ = asymptotic gas temperature (°C)
T_o = initial surface temperature (°C)
T_s = surface temperature measured by TLC (°C)
TLC = thermochromic liquid crystal
U_h = overall relative uncertainty (%)
x = coordinate (m)
y = coordinate (m)
z = coordinate coinciding with the brake rotor's shaft (m)

Greek Symbols

α = thermal diffusivity (m^2/s)
Δ = difference operator
ε = porosity
ρ = solid material density (kg/m^3)
ρ_{SA} = rotor surface area density (m^2/m^3)
τ = time constant (s)
τ_j = dummy time variable (s)
erfc(…) = complementary error function

References

[1] McPhee, A. D., and Johnson, D. A., 2008, "Experimental Heat Transfer and Flow Analysis of a Vented Brake Rotor," Int. J. Therm. Sci., **47**(4), pp. 458–467.
[2] Limpert, R., 2011, *Brake Design and Safety*, SAE International, Warrendale, Pittsburgh, PA, p. 58 .
[3] Abbas, S. A., Cubitt, N. J., and Hooke, C. J., 1969, "Temperature Distributions in Disc Brakes," Proc. Inst. Mech. Eng., **184**(1), pp. 185–194.
[4] Ramachandra Rao, V. T. V. S., Ramasubramanian, H., and Seetharamu, K. N., 1989, "Analysis of Temperature Field in Brake Disc for Fade Assessment," Wärme-Und Stoffübertragung (Heat Mass Transfer), **24**(1), pp. 9–17.
[5] Gerrard, M. D., 1993, "Thermal Distortion of Ventilated Brake Discs," M.Sc. thesis, Durham University, Durham, UK.
[6] Mackin, T. J., Noe, S. C., Ball, K. J., Bedell, B. C., Bim-Merle, D. P., Bingaman, M. C., Bomleny, D. M., Chemlir, G. J., Clayton, D. B., Evans, H. A., Gau, R., Hart, J. L., Karney, J. S., Kiple, B. P., Kaluga, R. C., Kung, P., Law, A. K., Lim, D., Merema, R. C., Miller, B. M., Miller, T. R., Nielson, T. J., O'Shea, T. M., Olson, M. T., Padilla, H. A., Penner, B. W., Penny, C., Peterson, R. P., Polidoro, V. C., Raghu, A., Resor, B. R., Robinson, B. J., Schambach, D., Snyder, B. D., Tom, E., Tschantz, R. R., Walker, B. M., Wasielewski, K. E., Webb, T. R., Wise, S. A., Yang, R. S., and Zimmerman, R. S., 2002, "Thermal Cracking in Disc Brakes," Eng. Failure Anal., **9**(1), pp. 63–76.
[7] Limpert, R., 1975, "The Thermal Performance of Automotive Disc Brakes," SAE Paper No. 750873.
[8] Newcomb, T. P., and Millner, N., 1965, "Cooling Rates of Brake Drums and Discs," Proc. Inst. Mech. Eng., **180**(Pt 2A, 1), pp. 191–205.
[9] Barigozzi, G., Perdichizzi, A., Paccchiana, P., and Goller, R., 2005, "Aero-Thermal Characteristics of an Automotive CCM Vented Brake Disc," SAE Paper No. 2005-01-3930.
[10] Wallis, L. M., 2003, "A Comparison of Bi-Directional Disc Brake Rotor Passage Designs," Ph.D. dissertation, The University of New South Wales, Sydney, Australia.
[11] Wallis, L., Leonardi, E., Milton, B., and Joseph, P., 2002, "Air Flow and Heat Transfer in Ventilated Disc Brake Rotors With Diamond and Tear Drop Pillars," Numer. Heat Transfer, Part A, **41**(6–7), pp. 643–655.
[12] Barigozzi, G., Cossali, G. E., Perdichizzi, A., Boden, A., and Paccchiana, P., 2002, "Experimental Investigation of the Mean and Turbulent Flow Characteristics at the Exit of Automotive Vented Brake Discs," SAE Paper No. 2002-01-2590.
[13] Lakshminarayana, B., 1996, *Fluid Dynamics and Heat Transfer of Turbomachinery*, Wiley, New York, p. 654.
[14] Barigozzi, G., Perdichizzi, A., and Donati, M., 2008, "Combined Experimental and CFD Investigation of Brake Discs Aero-Thermal Performances," SAE Paper No. 2008-01-2550.
[15] Palmer, E., Mishra, R., and Fieldhouse, J., 2008, "A Computational Fluid Dynamic Analysis on the Effect of Front Row Pin Geometry on the Aero-Thermodynamic Properties of a Pin-Vented Brake Disc," Proc. Inst. Mech. Eng., Part D, **222**(7), pp. 1231–1245.
[16] Mew, T. D., Kang, K. J., Kienhöfer, F. W., and Kim, T., 2015, "Transient Thermal Response of a Highly Porous Ventilated Brake Disc," Proc. Inst. Mech. Eng., Part D, **229**(6), pp. 674–683.
[17] Yan, H. B., Mew, T., Lee, M. G., Kang, K. J., Lu, T. J., Kienhöfer, F. W., and Kim, T., 2015, "Thermofluidic Characteristics of a Porous Ventilated Brake Disk," ASME J. Heat Transfer, **137**(2), p. 022601.
[18] Metzger, D. E., and Larson, D. E., 1986, "Use of Melting Point Surface Coatings for Local Convective Heat Transfer Measurements in Rectangular Channel Flows With −90 Deg Turns," ASME J. Heat Transfer, **108**(1), pp. 48–54.
[19] Metzger, D. E., Bunker, R. S., and Bosch, G., 1991, "Transient Liquid Crystal Measurement of Local Heat Transfer on a Rotating Disk With Jet Impingement," ASME J. Turbomach., **113**(1), pp. 52–59.
[20] Gillespie, D. R. H., Wang, Z., Ireland, P. T., and Kohler, S. T., 1998, "Full Surface Local Heat Transfer Coefficient Measurements in a Model of an Integrally Cast Impingement Cooling Geometry," ASME J. Turbomach., **120**(1), pp. 92–99.
[21] Ireland, P. T., Neely, A. J., Gillespie, D. R. H., and Robertson, A. J., 1999, "Turbulent Heat Transfer Measurements Using Liquid Crystals," Int. J. Heat Fluid Flow, **20**(4), pp. 355–367.
[22] Ireland, P. T., and Jones, T. V., 2000, "Liquid Crystal Measurements of Heat Transfer and Surface Shear Stress," Meas. Sci. Technol., **11**(7), pp. 969–986.
[23] Ekkad, S. V., and Han, J. C., 2000, "A Transient Liquid Crystal Thermography Technique for Gas Turbine Heat Transfer Measurements," Meas. Sci. Technol., **11**(7), pp. 957–968.
[24] Yan, Y., and Owen, J. M., 2002, "Uncertainties in Transient Heat Transfer Measurements With Liquid Crystal," Int. J. Heat Fluid Flow, **23**(1), pp. 29–35.
[25] Newton, P. J., Yan, Y., Stevens, N. E., Evatt, S. T., Lock, G. D., and Owen, J. M., 2003, "Transient Heat Transfer Measurements Using Thermochromic Liquid Crystal—Part 1: An Improved Technique," Int. J. Heat Fluid Flow, **24**(1), pp. 14–22.
[26] Poser, R., von Wolfersdorf, J., and Lutum, E., 2007, "Advanced Evaluation of Transient Heat Transfer Experiments Using Thermochromic Liquid Crystals," Proc. Inst. Mech. Eng., Part A, **221**(6), pp. 793–801.
[27] Steurer, A., Poser, R., von Wolfersdorf, J., and Retzko, S., 2019, "Application of the Transient Heat Transfer Measurement Technique Using Thermochromic Liquid Crystals in a Network Configuration With Intersecting Circular Passages," ASME J. Turbomach., **141**(5), pp. 1–9.
[28] Baughn, J. W., Anderson, M. R., Mayhew, J. E., and Wolf, J. D., 1999, "Hysteresis of Thermochromic Liquid Crystal Temperature Measurement Based on Hue," ASME, J. Heat Transfer, **121**(4), pp. 1067–1072.
[29] Mills, A. F., 1995, *Basic Heat and Mass Transfer*, Irwin, Chicago, IL, p. 147.
[30] Carslaw, H. S., and Jaeger, J. C., 1959, *Conduction of Heat in Solids*, 2nd ed., Oxford University Press, London, pp. 306–494.
[31] Schneider, P. J., 1955, *Conduction Heat Transfer*, Addison-Wesley Publishing Company Inc, Reading, MA, pp. 263–265.
[32] Kim, T., 2004, "Fluid-Flow and Heat-Transfer in a Lattice-Frame Material," Ph.D. dissertation, University of Cambridge, Cambridge, UK.
[33] Kim, T., Hodson, H. P., and Lu, T. J., 2004, "Fluid-Flow and End-Wall Heat Transfer Characteristics of an Ultralight Lattice-Frame Material," Int. J. Heat Mass Transfer, **47**(6–7), pp. 1129–1140.
[34] Kays, W. H., 1966, *Convective Heat and Mass Transfer*, McGraw-Hill Book Company, New York, pp. 133–137.
[35] Myers, G. E., 1987, *Analytical Methods in Conduction Heat Transfer*, Genium Publishing Corp., New York, pp. 153–163.

[36] Coleman, H. W., and Steel, W. G., 1999, *Experimentation and Uncertainty Analysis for Engineers Second Edition*, Wiley, New York, p. 10.
[37] Moffat, R. J., 1982, "Contributions to the Theory of Single-Sample Uncertainty Analysis," ASME J Fluids Eng., **104**(2), pp. 250–258.
[38] Moffat, R. J., 1988, "Describing the Uncertainties in Experimental Results," Exp. Therm. Fluid Sci., **1**(1), pp. 3–17.
[39] Gillespie, D. R. H., 1996, "Intricate Internal Cooling Systems for Gas Turbine Blading," D.Phil. thesis, University of Oxford, Oxford, UK.
[40] Schlichting, H., and Gersten, K., 2000, *Boundary Layer Theory*, Springer, Heidelberg, pp. 18–23.
[41] Stephens, A., Watkins, S., and Dixon, C., 2003, "Aerodynamic Testing of a Vented Disc Brake," SAE Paper No. 2003-01-0932.